Non-Gaussian Distributions of TOA SW Flux as Observed by MISR and CERES

Jae N. Lee[1,2] and Dong L. Wu[2]

[1]Joint Center for Earth Systems Technology, University of Maryland, Baltimore County, Baltimore, Maryland
[2]NASA Goddard Space Flight Center, Greenbelt, Maryland

Key Points:

- The probability density function of the TOA SW flux is not normally distributed but positively skewed, with a near-global median value of ~3 W/m^2 less than the mean.

- Hemispheric asymmetry exists with the 10:30 AM local time TOA SW observations from Terra platform. SH reflects about 1 – 4 W/m^2 more SW flux than NH, with the MISR and CERES Single Scanner Footprint (SSF1deg) products observed from Terra.

- While the characteristics of the MISR and CERES SW fluxes are broadly agree with each other, differences in the regional PDF from the two SW fluxes are substantially different over high cloud regions and high altitude regions.

Abstract

The Top of Atmosphere (TOA) shortwave (SW) flux, converted from Terra Multi-angle Imaging SpectroRadiometer (MISR) narrow band albedos, is compared with that measured from Clouds and the Earth's Radiant Energy System (CERES). We describe the probability density function (PDF) of the monthly TOA SW flux and how the statistical third moment, skewness, can impact the quantification of the flux. The PDF of the SW flux is not normally distributed but positively skewed. In both sets of observations, the near-global (80S-80N) median value of the SW flux is ~3 W/m^2 less than the mean value, due to the positive skewness of the distribution. The near-global mean TOA SW flux converted from MISR is about 7 W/m^2 (~7%) less than CERES measured flux during the last two decades. Surprisingly, hemispheric asymmetry exists with TOA SW observations from Terra platform. SH reflects 3.92 W/m^2 and 1.15 W/m^2 more mean SW flux than NH, from MISR and CERES Single Scanner Footprint products, respectively. We can infer that the offsetting by morning clouds in the SH is greater than the effect of hemispheric imbalance of SW flux caused by different land masses in two hemispheres. While the characteristics of the two SW fluxes broadly agree with each other, differences in the regional PDF from two different SW fluxes are substantially different over high cloud regions and high altitude regions. Our analysis shows that some parts of the different skewness from two measurements may be attributed to the different calibration of the radiance anisotropy over high cloud scenes.

Plain Language Summary

In this work, we describe the non-Gaussian probability density functions (PDFs) of the Top of Atmosphere (TOA) reflected shortwave (SW) flux. For non-Gaussian PDFs, the frequency of occurrence is not symmetric with respect to the mean. The TOA SW PDFs are relatively thick in the left tail, because there exists a low boundary of zero reflectance when the Earth don't get solar insolation during the polar nights. In comparison of two satellite measurements, we show that how the statistical third moments of the TOA SW flux can impact the quantification of the averaged flux. Gaussian distributions are naturally assumed in atmospheric data analysis. This, however, is not always true for the TOA SW flux distribution.

To quantify the global TOA SW flux, reliable and consistent satellite measurement is required. The two instruments, MISR and CERES, on the Earth Observing System Terra satellite (launched in December of 1999) offer a rare opportunity to observe the TOA reflected SW flux from the same constellation. Hemispheric asymmetry exists in the 10:30 AM local time TOA SW observations from Terra platform. SH reflects about 1 – 4 W/m^2 more SW flux than NH, with the MISR and CERES Single Scanner Footprint (SSF1deg) products observed from Terra.

1 Introduction

Quantifying the amount of solar insolation reflected back to space at the top of the atmosphere (TOA) is pivotal for an assessment of Earth's radiation balance (Trenberth , 2009; Stephens et al. 2012; Wild et al., 2015; Loeb and Wielicki 2015; L'Ecuyer 2017). This reflected SW energy is initially forced by diurnal and seasonal variations of the incoming solar insolation. Caused by the obliquity of the Earth, each hemisphere receives more solar radiation during its summer when the hemisphere is tilted toward the Sun, and less during winter when it is tilted away. Distribution of TOA reflected SW flux (TOA SW flux) is a mixture of complex multiple processes of surface and atmospheric reflection from different types of surface and atmospheric conditions. Furthermore, the hemispheric asymmetry of the global land and ocean masses builds on additional complexity in characterization of the TOA SW flux. The 11-year solar cycle variation of the solar insolation also can be factored in the decadal variations, however, the effect of solar cycle is expected to be negligible as it's magnitude is less than 0.01% (Kopp and Lean, 2011).

Besides the accurate assessment of mean (μ) and standard deviation (σ) of the flux, a careful examination on the normality of TOA SW flux distribution is meaningful because the TOA SW flux distribution reflects the hemispheric asymmetry of solar insolation and land masses. A Gaussian, or Normal distribution is a type of probability distribution for a random variable, as the probability density function (PDF) is symmetric on either side from the mean with no skewness. Partly due to the central limit theorem (Feller, 1971) which states the average of many observations of a random variable approaches a normal distribution, the mean of the normal distributions are commonly used to represent observed and modeled large scale atmospheric and oceanic variables. However, in fact, normality of the distribution is one of the underlying assumptions in data analysis. When PDFs are deviated from the normal distribution, they are not well characterized by the μ and σ. Not like a normal distribution, it would be insufficient to deduce the states of tail probabilities even if the changes of μ and σ are accurately estimated. The skewness of the distribution can cause a complexity in quantifying trends (Sardeshmukh et al., 2015) because the shape of the heavy tail, high reflected flux in TOA SW case, may not be preserved with fastly vanishing high-latitude snow and ice.

In this work, we describe the non-Gaussian probability density functions of TOA SW flux, in comparison of two satellite measurements from MISR and CERES, and how the statistical third moments of the TOA SW flux can impact the quantification of the globally averaged flux. We also quantify the hemispheric differences of TOA SW flux between NH and SH and how they are dependent on observing constellation of Terra and Aqua.

To quantify the global climatology of TOA SW flux, reliable and consistent satellite measurement is required. The two instruments, MISR and CERES, on the Earth Observing System Terra satellite (launched in December of 1999) offer a rare opportunity to observe the TOA reflected SW flux from the same constellation. Since no space-based measurement, so far, can measure radiances in all viewing angles simultaneously, the radiance-to-flux conversion has been recognized as a major source of uncertainty in the satellite derived TOA SW flux (Loeb et al., 2006). Even after considerable improvements in Angular Distribution Models (ADMs), challenges are still remaining in the radiance to flux conversion, due to ADMs' strong dependence on clouds and high-albedo surfaces (Loeb et al.; 2007; 2018; Gristey et al., 2021; and references therein).

The MISR instrument provides information on bidirectional reflectance anisotropy (Diner et al., 2005) and inconsistency between the MISR and CERES fluxes can be largely attributed to limitations in the integration of bidirectional reflectance and ADMs (Loeb et al., 2006). Over the overcast ocean scenes within 75S-75N, the uncertainty in the MISR albedos due to narrow-to-broadband albedo conversion is ~2%. The difference between the MISR and CERES albedos due to the angular distribution model (ADM) is estimated to be ~4% (Sun et al., 2006).

2 Data

2.1 MISR

MISR's arrangement of nine cameras provides near-simultaneous measurements of reflective SW radiances from multi-angle views in four spectral bands (Diner et al., 1998). Reflected SW spectral radiances are measured at nadir and at 26.1°, 45.6°, 60° and 70.5° forward and aft of nadir along the satellite track, in blue (446±21nm), green (558±15nm), red (672±11nm), and near-infrared (866±20nm) bands. By deriving albedos from nine angular measurements, MISR has an advantage of retrieving accurate albedos for inhomogeneous clouds (Diner et al., 2005; MISR ATBD, https://eospso.gsfc.nasa.gov/sites/default/files/atbd/atbd-misr-08.pdf).

MISR produces three TOA spectral albedo products; local, restrictive, and expansive albedos. Local albedo estimates the reflected flux passing through an unobscured 2.2 km domain reflecting level of reference altitude. The restrictive albedo is an estimate of the reflected flux which originates from the reflecting surfaces within 35 km domain. The expansive albedo is an estimate of the flux passing through the TOA regardless of where it is reflected.
We used the restrictive albedos in this study, since it is a useful measure of scene-dependent properties and most analogous to the CERES determination of the TOA albedo from a single view.

The methodology applied to compute MISR broadband albedo involves a regression of 4 spectral narrow band albedos onto CERES broadband albedo (Sun et al., 2006). Then broadband MISR restrictive albedo (α) is converted to TOA SW flux by multiplying incident solar insolation (S0) at a given time and location, i.e., TOA SW flux = $\alpha \cdot S0$. Incident solar insolation, S0, is acquired from CERES SSF1deg product at a given time and location.

In this study, we utilized the restrictive broadband albedos from MISR Level-3 albedo product (Diner, 2009), since March 2000 to December 2020, from NASA Atmospheric Science Data Center (https://asdc.larc.nasa.gov/documents/misr/version/pge12b.html). Given the sampling nature of the MISR observation, we used monthly mean data products.

2.2 CERES

The CERES Edition 4.1 monthly mean 1 degree gridded Single Scanner Footprint (SSF1deg) TOA SW flux products from Terra and Aqua satellite (Doelling, 2015) and Energy Balanced and Filled (EBAF) products (Doelling, 2019) are analyzed to be compared with converted broadband MISR flux. The SSF1deg product began in March 2000 and provides global coverage sampled only at specific times of the day (Doelling et al., 2013). As well as MISR, the CERES instrument on EOS Terra measures TOA SW flux in a sun-synchronous ascending orbit with an equator crossing time of near 10:30 AM local time. The CERES albedo retrieval is based on a set of combined empirical and theoretical scene-dependent ADMs (Kato, 2005; Loeb et al., 2005; Loeb et al., 2009; Su et al., 2015a; 2015b; Ham et al., 2015; and references there in). The selection of ADMs depends on the cloud types and a cloud parameter which is determined from the cloud fraction, optical depth, cloud height, and phase of clouds.

In this study, we focused on examining the consistencies and differences of the TOA SW flux from the MISR and CER_SSF_Terra-FM1-MODIS_Edition4A datasets. Where MISR data is not available in high latitudes, we also omitted CERES data for a fair comparison. We obtained the CERES SSF1deg monthly TOA SW and cloud height data from (https://ceres-tool.larc.nasa.gov/ord-tool/jsp/SSF1degEd41Selection.jsp).

3 Results

3.1 Non-Normality of the TOA SW flux

In this section, we describe the non-Gaussian distributions of TOA SW flux, in comparison of two satellite measurements from MISR and CERES. As shown in Figure 1, the PDFs of MISR and CERES TOA SW flux are not only non-Gaussian, but are distinctly skewed distributions which have more population of the data on the right side of the maximum population. The PDFs of the monthly broadband TOA SW flux from MISR and CERES are shown in Figure 1(a), where the area under the PDF accounts for the near-global (80S - 80N) distribution of monthly mean TOA SW flux at each 1° by 1° grids. The distribution of the data indicates that monthly mean TOA SW flux extends from 0 to 410 W/m^2.

The PDFs of broadband flux show one major peak at 58 W/m^2 and 65 W/m^2 for MISR and CERES, respectively. While the general features of PDFs of the near-global TOA SW distribution from the two observations are in good agreement with ~7 W/m^2 offset at the peak, they commonly show that SW fluxes are obviously not normally distributed. The right side of the distribution is heavily tailed with high reflectance values from snow and ice, but the left side of the distribution has no tails. The PDFs are relatively thick in the left tail, because TOA SW flux cannot be negative with a low boundary of zero reflectance when they don't get solar insolation during the polar nights.

Similarly, the PDFs of the four narrow band MISR TOA SW fluxes centered at blue (C1: 446±21nm), green (C2: 558±15nm), red (C3: 672±11nm), and near-infrared (C4: 866±20nm) are shown in Figure 1(b). The four spectral PDFs also show similar skewed non-Gaussian features.

For a Gaussian, or Normal distribution, the PDF is symmetric on either side from the mean. Without any prior assumptions, the TOA SW distributions are deviated from the normal distribution, they are not well characterized by the μ and σ. Not like a normal distribution, it would be insufficient to deduce the changes in tail probabilities from the μ and σ, even if the changes of μ and σ are accurately estimated.

Skewness is a measure of the asymmetry of the probability distribution about its mean. Conventionally, positive skewness indicates that more populations of data are located on the right tail from the maximum population. Reflecting the positive skewness, the TOA SW flux distributions show that more populations are present on the right side of the distribution where the fluxes are larger than the mean or median. The right tail of the SW flux distribution is extremely important, since the high flux greater than 300 W/m^2 is from the Arctic and Antarctic region over high albedo snow and ice surface. The right tail of the SW flux is also related to cloud properties and the estimating the average flux without considering cloud types may cause systematic biases (Barket et al., 1996). The skewness of the distribution can add complexity in quantifying global TOA SW climatologies and trends because the shape of the distribution may not be preserved with a changing environment. For example, fastly vanishing high-latitude snow and ice can cause a thickening of the right tail without affecting the left tail of the distribution.

Figure 2 is a schematic of the MISR TOA SW flux, which shows the PDF deviated from the normal distribution. The mean and the standard deviation of the not area-weighted near-global SW flux from MISR (80S - 80N) is 98.6 W/m^2, and 66.19 W/m^2, respectively. The global (90S-90N), annual mean all-sky TOA SW flux from CERES Energy Balanced and Filled (EBAF) data was 99.7 W/m^2, which is equivalent to a global albedo of 0.293 (Stephens et al., 2015).

The red curve of the plot is the best-fit normal distribution with the same mean and standard deviation from MISR. The yellow curve is a normal distribution with a mean at the mode, where the most population is located. The blue curve is a best-fit lognormal distribution using the log of TOA SW flux values. The median of the distribution is 83.68 W/m^2, which is ~15 W/m^2 less than the mean. While the TOA SW flux distribution is deviated from the normal distribution, it is rather close to the lognormal distribution with mean (m) and standard deviation (v) of 4.46 and 0.63 W/m^2, respectively. The lognormal distribution can be potentially utilized to estimate the true mean and variance of the TOA SW flux in future work, however, the conversion of the lognormal to normal distribution is very sensitive to the parameters of the lognormal distribution, i.e. m and v., since the true mean (μ) and standard deviation (σ) of the original distribution can be acquired from the exponential function of m and v.

We generated climatologies (2001-2020) for MISR and CERES TOA SW flux on a 1°x1° spatial scale, by taking not only the monthly mean averages, but also taking median values of SW flux at each grid over a period under study. To find the region where the temporal distribution is deviated from the normal distribution, we estimated the difference of climatology of the mean and the median by subtracting the mean climatology from the median climatology, i.e. MEDIAN - MEAN at each grid point. Figures 3(a)-(b) show the spatial distributions of the difference between the median climatology and the mean climatology within 60S - 60N from MISR and CERES, respectively. The similarities of each figure from two different measurements indicate that the difference between median and mean is a real common feature, not originating from the artifacts of the measurements. The largest difference is shown over the Deccan Peninsula, a dry and elevated plateau where the large annual variation of precipitation and vegetation is evident due to the strong Monsoon.

Figure 3(c)-(f) show respectively the spatial distributions of the skewness and kurtosis of the TOA SW flux distribution from the MISR and CERES observations. The skewness could be reduced from the daily to monthly averages in accord with the central limit theorem, but it still remains strongly positive in the central Southern Pacific. Regions of large positive skewness generally coincide with regions of large positive kurtosis. Very high skewness and kurtosis values concur over the central Southern Pacific ocean that contain less amounts of clouds resulting from less convective activity in the middle of the Inter tropical convergence zone (ITCZ) and South Pacific Convergence Zone (SPCZ).

The PDFs of the SW flux show interesting results related to the nature of the flux and the instruments that measure the flux. In Figure 4, the PDFs of the flux over Deccan Peninsula and central Southern Pacific Ocean clearly show distinct features in each area.

Over the Deccan Peninsula (Figure 4(a)), the PDFs show a long and thick right tail in both observations. Over the central Southern Pacific ocean (Figure 4(b)), the both PDFs show high skewness and high kurtosis but two observations show differences in the mean and median. The mean and the median of the MISR SW flux is ~ 6 W/m^2 (~11%) and ~7 W/m^2 (~14%) lower than that of CERES, respectively. The SW flux distributions over this Pacific region are leptokurtic, as they show highly non-Gaussian features with large values of kurtosis about 14 (MISR) and 22 (CERES). The leptokurtic distribution has long tails that asymptotically approach zero more slowly than a Gaussian, therefore produces more outliers than the normal distribution. With higher skewness and kurtosis than normal distribution, the SW flux has a larger population on the right tail caused by high reflective cloudiness.

Over the high skewness and kurtosis region in the central Southern Pacific ocean, we find negative correlation between skewness and SW flux values, as shown in Figure 5. The linear correlation coefficients between skewness and SW flux is -0.72 and -0.73 for MISR and CERES, respectively. Besides, the skewness abruptly increases where the SW flux is less than 60 W/m^2 with relatively less clouds over the Pacific region. We can infer this negative correlation as skewness can be reduced by clouds by their random scattering of the lights. This result corroborates with Datseris and Stevens (2021) that the zonal and temporal distribution of cloud contribution to atmospheric albedo is mostly attributable to the contribution of cloud fraction.

3.2 Seasonal cycle and hemispheric asymmetry of annual mean SW

The seasonal cycle of satellite-based global mean albedo and reflected fluxes has been discussed in a number of previous works (Kato, 2009; Stephens et al., 2015;2016; Song et al., 2018; Datseris & Stevens, 2021; and reference therein). What is different about this work from earlier studies is that the zonal and temporal median is also shown besides the temporal average of the zonal mean with MISR and CERES SSF data. The seasonal cycles shown in Figure 6 are the mean and median of 20 annual cycles (2001-2020) from MISR and CERES SSF data on Terra satellite. Monthly zonal mean and median fluxes computed from 20 years for each month of the year and area weighted and averaged over a given region. The TOA SW flux observations inferred from MISR and CERES produce consistent features of the seasonal cycle of SW flux, as shown in Figure 6.

The seasonal cycle of the SW flux generally follows the seasonal cycle of the solar insolation, based on Sun-Earth distance and inclination angle changes, which determine the local incoming solar insolation at a given time of the year. Strong hemispheric asymmetry is evident that the seasonal cycle amplitude of global mean solar insolation is more than one magnitude smaller

(25.3 W/m^2) than those of NH mean (243.9 W/m^2) and SH mean (289.3 W/m^2), when they are calculated with solar insolation appeared in CERES SSF product. The reduced amplitude of the near-global seasonal cycle of SW flux (Figure 6(a)) compared to the that of NH and SH (Figure 6(b)-(c)) illustrates how the hemispheric asymmetry contributes to the global average of the reflected fluxes.

Furthermore, the amount of the reflected SW flux also depends on the atmospheric and surface properties. The global mean SW flux is a combination of the flux over land and ocean, therefore, the seasonal cycle of SW flux is also a combination of land and ocean, depending on the seasonal cycle of cloudiness, vegetation, snow, and ice. The differences of the area weighted near-global mean and median values (mean - median) are about 3 W/m^2 in both observations due to the over-weighted mean with respect to median, originating from the positive skewness.

The amplitudes of the annual cycle over the ocean (Figure 6(h)-(i)) is larger than those over land (Figure 6(e)-(f)) in both hemispheres. The seasonal cycle of land surface albedo has summertime minimum resulting from the vegetation and wintertime maximum resulting from the brighter snow covered lands. In both land and ocean cases, the amplitudes of the annual cycle in the SH (Figure 6(f)-(i)) are ~20W/ m^2 greater than those in the NH. The large amplitude of the annual cycle over the SH ocean (Figure 6(i)) can be attributed to the reflection from midlatitude clouds over the storm track during the austral winter.

Despite the strong seasonal variations in the reflected SW flux, its annual means for the NH and SH are nearly equal. Whether this is accidental or intrinsic to the Earth's climate system or variable with time is subject to research debate (Datseris and Stevens, 2021). Different from earlier studies with CERES EBAF SW flux, we analyzed the CERES Terra, Aqua, and EBAF data separately. Annually averaged TOA SW flux (W/m^2) during 2001-2020 is summarized in Table 1 at a given region.

For the Terra-only MISR and CERES SW flux, observed at ~10:30 AM local time, the hemispheric asymmetry is evident that the SH reflects 3.92 W/m^2 and 1.15 W/m^2 more mean SW flux than the NH, respectively. For the Aqua-only CERES SW flux, obtained at ~1:30 PM local time, the hemispheric asymmetry has the opposite sign, which largely offsets the SH-NH difference in Terra flux to produce a nearly equal TOA SW flux in both hemispheres.

The hemispheric symmetry in the annual and long-term mean TOA SW flux has a significant implication for Earth's energy balance, as any inequality would require a compensation from the LW flux or inter-hemispheric energy transfers (e.g., meridional oceanic heat transfer). Compared to the NH, the SH has much more ocean which is less reflective than land, so the SH is expected to reflect less than the NH. However, the hemispheric symmetry of the SW flux with equal amount of reflected flux in each hemisphere has been reported and explained by increased SH clouds offsetting the greater reflection from the NH land masses. We can infer that this offsetting by morning clouds, measured at 10:30AM local time, overwhelms the effect of hemispheric imbalance of land and ocean masses between two hemispheres. The marine stratocumulus has a maximum thickness during the morning and a minimum thickness during the afternoon (Gristey et al., 2017a). We can speculate that the high SW flux in the SH from the Terra observation is due to the thick morning marine stratocumulus, since this type of clouds are more widespread in the SH than the NH. Similarly, less SW is reflected in the SH, by the time of Aqua overpass in the afternoon when those clouds have dissipated. More details on the difference between NH and SH is further discussed in the discussions section.

3.3 Height-dependent CERES-MISR differences

The multi-year (2001–2020) TOA SW median climatology from MISR and CERES agree fairly well with each other over non-polar regions, with the bias close to 7 W/m^2 and the RMS error of 8.5 W/m^2. As shown in Figure 7, the differences, CERES - MISR, are in general positive everywhere except Greenland and SH high latitude regions, since the near-global mean TOA SW flux from CERES is close to 7 W/m^2 greater than that from MISR. Black and red contour lines in the figure indicate high elevation area (z>2km) and high cloud regions (cloud height> 9km), respectively.

It is interesting that the largest differences up to 30 W/m^2 are observed over tropical high cloud regions where monthly mean cloud top heights are higher than 9km. Regions where the elevation is higher than 2km also show large differences. The cloud top heights are acquired from the same CERES SSF product. The world terrain reference (World Geodetic System 1984) model is used in this study, which is the same data set used by the Terra MISR and CERES algorithms.

While TOA SW flux inferred from multiple directions is ideally expected to be independent of satellite viewing geometry by definition, two fluxes from multiple directions over the same scene are not identical due to differences in geometry and algorithm. Differences between the two measurements indicate that there exist uncertainties in spatial and temporal matching, narrow-to broadband conversion, parallax effects, and algorithms for the angular corrections of the radiance field. Each instrument's algorithms, MISR's Bidirectional Reflectance Factor (BDF) corrections and CERES ADMs, account for the angular distribution of the radiance, which strongly dependent on the physical and optical properties of each scene for a given surface type, cloud fraction, cloud/aerosol optical depth, cloud phase, as well as the illumination angle (Loeb et al., 2006).

The uncertainties of the TOA albedos from CERES and MISR have been carefully estimated in previous works. Over the overcast ocean scenes within 75S-75N, the uncertainty in the MISR albedos due to narrow-to-broad band albedo conversion is ~2% (Sun et al., 2006). Similarly, the difference between the MISR and CERES albedos due to the angular distribution model (ADM) is estimated to be ~4%. Over the Arctic overcast scene, the difference between the two measured albedos are mostly due to differential BRF anisotropic corrections, and it is estimated to be less than 4% when the solar zenith angle (SZA) is less than 70°, while it increases up to 13.5% when the SZA is greater than 80° (Zhan et al., 2018).

We further classified the PDFs of MISR and CERES SW flux (W/m^2) over the ocean (60S-60N) for different cloud heights from 1 to 12 km, as shown in Figure 8. As the cloud heights increase, the difference between two observations grows. Besides, the PDFs are getting close to the normal distribution and the skewness approaches to zero over high cloud regions. This is also shown in a graph of the difference between CERES and MISR (%) and skewness of the PDFs as a function of cloud heights (Figure 9).

Besides the cloud properties, i.e., cloud fraction, optical depth, and phase of clouds, magnitude of the SW also depends on three-dimensional (3D) structure of clouds (Ham et al., 2015; Singer et al., 2021). The effects of 3D cloud morphology on SW reflectance, which are not fully resolved in radiative transfer algorithm, may cause additional bias in two measurements for high cloud scenes.

4 Discussions

4.1 Hemispheric asymmetry in SW flux

Diurnal sampling plays an important role in the hemispheric asymmetry, SH-NH differences, of the TOA SW flux. As reported in the previous section, this difference is positive in the Terra observations (i.e., MISR and CERES), but negative in the Aqua CERES. As shown in Figure 10, the CERES EBAF result is approximately the average of the Terra and Aqua observation, while different SW flux data show a similar interannual variation. To assess the degree to which the hemispheric symmetry is sensitive to the missing coverage at high latitudes, we compared the annual mean EBAF CERES SW fluxes with various missing portions of high-latitude coverage. Although the interannual variations tend to track each other, the SH-NH differences are relatively small for the global averages with missing latitudes 70^o poleward. But the differences start to increase as more polar latitudes are not covered. For example, if the coverage misses 60^o poleward, the SH-NH differences can be ~2 W/m^2 with the SH flux being lower, largely because of the extensive coverage from clouds and Antarctic ice. From this analysis we concluded that the missing latitude coverage cannot explain the large difference between MISR and CERES observations from Terra. The MISR-CERES difference is likely due to the underlying assumptions used in their algorithms. For MISR, it requires to convert four narrow-band fluxes to obtain the broadband SW flux, although it measures these narrow-band fluxes from multiple angles along the orbital track. On the other hand, CERES needs to convert the broad-band radiance from a single scan to the full hemispheric SW flux, which requires knowledge of angular distribution models (ADMs) for each scene. In both MISR and CERES SW retrievals, scene type classification is required to carry out the narrow-to-broad-band (MISR) and radiance-to-flux (CERES) conversion.

Characteristics of the Terra and Aqua CERES sampling are described by Figure 11 in which the NH and SH exhibit very different local time coverages. Thus, the diurnal variations of TOA SW are critical for understanding and interpreting the hemispheric symmetry. If the SW diurnal variation is symmetric about noon, the average of Terra and Aqua data would yield cancellation of the SH-NH asymmetric values observed by each satellite alone. However, if the diurnal variation is not symmetric with respect to noon, their average would not cancel the SH-NH differences. A recent study showed that the SW diurnal variation from the CERES EBAF is somewhat different to the one inferred from the DSCOVR/EPIC observation (Lim et al., 2021). In addition, the rate of daytime cloud fraction changes from DSCOVR/EPIC observations is not symmetric about noon either (Delgado-Bonal et al., 2021). The diurnal variation of albedo estimated from the Earth Radiation Budget Experiment (ERBE) also show that the albedo variations are not always symmetric with respect to noon due to variations of cloudiness throughout the day, which are asymmetric about noon (Rutan et al., 2014). The diurnal variations built in CERES EBAF are largely based on geostationary satellite observations, which cover latitudes up to 60^oN/S. Therefore, the uncertainty is likely high in the CERES EBAF data for the SW diurnal variation 60^o poleward. This is the region where the Terra and Aqua local time samplings differ most, as shown by Figure 11.

Our analysis result stresses the importance of diurnal sampling for the SW observations from future missions. Potential constellations of the satellite observations have been suggested to better resolve distinct diurnal signatures of the outgoing Earth radiation (Gristey et al., 2017b;

Hakuba et al., 2018; Swartz et al., 2019; and Mefta et al., 2021). As a continuation mission to CERES, NASA's Libera (https://lasp.colorado.edu/home/libera/) is planned to fly on the Joint Polar Satellite System-3 (JPSS-3) satellite (1:30 PM equator-crossing time) to maintain the long-term record of TOA radiative fluxes. The Libera's sampling will be similar to Aqua and would require a diurnal cycle model to obtain the daytime mean TOA SW flux. Without correcting the diurnal variation, the Libera's SH-NH difference would be similar to Aqua CERES observations seen in Figure 11.

4.2 Possible causes of the TOA SW skewness variations

We show that monthly mean TOA SW fluxes are obviously not normally distributed, but positively skewed as a mixture of fluxes from land and ocean. According to the central limit theorem, the average of many observations of a random variable approaches a normal distribution. However, in case of TOA SW observation, normality of the distribution is not acquired by taking an average for the monthly mean from the daily means. In global scale, the PDFs of SW flux are relatively thick in the left tail, because there exists a low boundary of zero reflectance when they don't get solar insolation during the polar nights. There also exists extreme high SW flux values above 400 W/m^2 over the summer polar regions.

The skewness of the SW flux distribution is not globally uniform, but changes depending on the selection of the spatial and temporal sampling. Besides, the large positive skewness of the observed TOA SW tends to occur in the extreme climatic regions where the seasonal variation of SW flux is relatively high. The PDF of the flux changes with season of the year, as the mean of the flux shows substantial seasonal variations (Figure 6) following the changes of the vegetation, clouds, ice, and atmospheric conditions. For example, the summertime PDF of the flux over land is quite different from the wintertime distribution (not shown) and the PDF over the land is different from that over the ocean. While the negative skewness is often shown over the low- to mid-latitude arid area over the African continent, the positive skewness is generally appeared over the ocean, as can be seen in Figure 3(c) - (d).

The PDFs of SW flux over high cloud regions are less skewed, compared to those over low cloud regions (Figure 8-9). Because the interannual variations in SW skewness are derived from variations of clouds, they are sensitive to the outlier years when the flux behaves abnormally, such as those from a strong ENSO event. Skewness often becomes significant in the cases where data variability has a lower or upper boundary. The data with a lower bound tend to have positive skewness while the data with an upper bound are often skewed left. The central Southern Pacific, where the annual mean CERES SWs are lowest and mostly from clear sky, the skewness is positively high. This is the region influenced strongly by the downward branch of both Hadley and Walker circulations on an annual basis, and is apparently sensitive to ENSO-induced circulation changes.

5 Conclusions

The comparison of twenty years of MISR and CERES observation offers an excellent opportunity to describe their similarities and differences in the TOA SW flux data sets from the two independent instruments on the same Terra platform. The analysis presented in this paper can be summarized in the following:

1. The PDFs of MISR and CERES SW fluxes commonly show that the TOA SW flux is not normally distributed but positively skewed. Distinct PDFs of the TOA SW flux can impact the quantification of the globally averaged flux. In both observations, the near-global median value of the SW flux is ~3 W/m^2 less than the mean of the flux, due to the positive skewness of the SW flux distribution. The near-global mean TOA SW flux converted from MISR narrow bands albedo is about 7 W/m^2 (<7%) less than CERES measured flux during the last two decades. Gaussian distributions are naturally assumed in atmospheric data analysis, as the central limit theorem states that distributions of random variables approach a normal distribution by taking their mean. This, however, is not always true for the TOA SW flux distribution. The PDFs of SW flux are relatively thick in the left tail, because there exists a low boundary of zero reflectance when they don't get solar insolation during the polar nights.

2. From Terra's AM observation (~10:30 AM local time), SH reflects ~1 and ~4 W/m^2 more SW flux than NH, with MISR and CERES SSF1deg product, respectively. Hemispheric mean SW flux depends on time of satellite measurement, since diurnal sampling plays an important role in determination of the daily mean. Different local time coverage in Terra and Aqua observation can cause sampling bias in estimating SW flux climatology in both hemispheres.

3. While the characteristics of the two SW fluxes broadly agree with each other, differences in the regional PDF from two different SW fluxes are substantially significant over high cloud regions and high altitude regions. Our analysis shows that some parts of the different skewness from two measurements may be attributed to different treatments of the radiance anisotropy over high cloud scenes. More analysis based on the the spatially and temporally collocated merged data set of CERES/MISR radiances (Loeb et al., 2006, Su et al., 2015a; 2015b, Zhan et al., 2018) and TOA albedo observed from Advanced Very High Resolution Radiometer (AVHRR) (Zhan and Liang, 2022) will further help to check the consistencies and uncertainties of the TOA SW flux measurements from the different instruments and to direct to the potential areas requiring improved solutions.

Acknowledgments

We thank the MISR and CERES Science Team for making the TOA albedo and SW flux data available on their websites, and three anonymous reviewers for their suggestions that helped to improve this manuscript. This work is supported by NASA's Sun-Climate research at Goddard Space Flight Center.

References

Barker, H. W., Wiellicki, B. A., & Parker, L. (1996). A Parameterization for Computing Grid-Averaged Solar Fluxes for Inhomogeneous Marine Boundary Layer Clouds. Part II: Validation Using Satellite Data, *J. of Atmos. Sciences*, *53*(16), 2304-2316. https://journals.ametsoc.org/view/journals/atsc/53/16/1520-0469_1996_053_2304_apfcga_2_0_co_2.xml

Datseris, G., & Stevens, B. (2021), Earth's albedo and its symmetry. *AGU Advances*, 2, e2021AV000440. https://doi.org/10.1029/2021AV000440.

Delgado-Bonal, A., Marshak, A., Yang, Y., & Oreopoulos, L. (2021), Global daytime variability of clouds from DSCOVR/EPIC observations. *Geophys. Res. Lett.*, 48, e2020GL091511. https://doi.org/10.1029/2020GL091511.

Diner, D. J., Beckert, J.C., Reilly, T.H., Bruegge, C.J., Conel, J.E., Kahn, R.A., Martonchik, J.V., Ackerman, T.P., Davies, R., Gerstl, S.A.W. (1998), Multi-angle Imaging SpectroRadiometer (MISR) instrument description and experiment overview. *IEEE Trans. Geosci. Remote Sens.*, *36*, 1072–1087.

Diner, D. J., Braswell, B. H., Davies, R., Gobron, N., Hu, J., Jin, Y., Kahn, R. A., Knyazikhin, Y., Loeb, N., Muller, J.-P., Nolin, A. W., Pinty, B., Schaaf, C. B., Seiz, G., and Stroeve, J., (2005), The value of multiangle measurements for retrieving structurally and radiatively consistent properties of clouds, aerosols, and surfaces, *Remote Sens. Environ*., 97, 495–518.

Diner, David. (2009). MISR Level 3 Component Global Albedo product in netCDF format covering a day - Version 6 [Data set]. NASA Langley Atmospheric Science Data Center DAAC. https://doi.org/10.5067/TERRA/MISR/MIL3DALN_L3.006

Doelling, D. R., N. G. Loeb, D. F. Keyes, M. L. Nordeen, D. Morstad, C. Nguyen, B. A. Wielicki, D. F. Young, M. Sun (2013), Geostationary Enhanced Temporal Interpolation for CERES Flux Products, *J. of Atmos. and Oceanic Technol.*, 30(6), 1072-1090. doi: 10.1175/JTECH-D-12-00136.1.

Doelling, David. (2015). CERES Level 3 SSF1deg-Month Terra-MODIS HDF file - Edition 4A [Data set]. NASA Langley Atmospheric Science Data Center DAAC. https://doi.org/10.5067/TERRA/CERES/SSF1DEGMONTH_L3.004A

Doelling, David. (2019). CERES Energy Balanced and Filled (EBAF) TOA and Surface Monthly means data in netCDF Edition 4.1 [Data set]. NASA Langley Atmospheric Science Data Center DAAC. https://doi.org/10.5067/TERRA-AQUA/CERES/EBAF_L3B.004.1

Feller, W., 1971. An introduction to probability theory and its applications, 2d. Ed., volume 2, New York, Wiley.

Gristey, J.J.; Chiu, J.C.; Gurney, R.J.; Morcrette, C.J.; Hill, P.G.; Russell, J.E.; Brindley, H.E. (2017a). Insights into the diurnal cycle of global Earth outgoing radiation using a numerical weather prediction model. *Atmos. Chem. Phys*., 18, 5129–5145.

Gristey, J. J., J. C. Chiu, R. J. Gurney,S.-C. Han, and C. J. Morcrette (2017b),Determination of global Earth outgoingradiation at high temporal resolutionusing a theoretical constellation ofsatellites, *J. Geophys. Res. Atmos*.,122,1114–1131, doi:10.1002/2016JD025514.

Gristey, J. J., W. Su, N. G. Loeb, T. H. Vonder Haar, F. Tornow, K. S. Schmidt, M. Z. Hakuba, P. Pilewskie, and J. E. Russell (2018), Shortwave Radiance to Irradiance Conversion for Earth Radiation Budget Satellite Observations: A Review*, Remote Sens*., 13(13), 2640.

Hakuba, M. Z. *et al*. (2019). Earth's Energy Imbalance Measured From Space, *IEEE Trans. Geosci. Remote Sens.*, vol. 57, no. 1, pp. 32-45, Jan. 2019, doi: 10.1109/TGRS.2018.2851976.

Ham, S.-H., Kato, S., Barker, H.W., Rose, F.G. and Sun-Mack, S. (2015), Improving the modelling of short-wave radiation through the use of a 3D scene construction algorithm. *Q. J. R. Meteorol. Soc.*, 141, 1870-1883. https://doi.org/10.1002/qj.2491.

Kato, S. Top-of-atmosphere shortwave broadband observed radiance and estimated irradiance over polar regions from Clouds and the Earth's Radiant Energy System (CERES) instruments on Terra (2005), *J. Geophys. Res.*, *110(D7),* D07202, doi: 10.1029/2004JD005308.

Kato, S. Interannual Variability of the Global Radiation Budget, (2009), *J. of Climate,* 22, 18 (2009): 4893-4907, doi: 10.1175/2009JCL1295.1.

Kopp, G., and Lean, J. L. (2011), A new, lower value of total solar irradiance: Evidence and climate significance, *Geophysical Research Letters*, 38, L01706, doi:10.1029/2010GL045777.

L'Ecuyer, T.S. (2017). Earth's Energy Balance. In International Encyclopedia of Geography: *People, the Earth, Environ. and Tech*., https://doi.org/10.1002/9781118786352.wbieg1132

Lim, Y.-K.; Wu, D.L.; Kim, K .-M.; Lee, J.N. (2021), An Investigation on Seasonal and Diurnal Cycles of TOA Shortwave Radiations from DSCOVR/EPIC, CERES, MERRA-2, and ERA5, *Remote Sens.*, 13, 4595. doi: 10.3390/rs13224595.

Loeb N. G., Kato S, Loukachine K, Manalo-Smith N. (2005), Angular distribution models for top-of-atmosphere radiative flux estimation from the Clouds and the Earth's Radiant Energy System instrument on the Terra satellite. Part I: Methodology. *J. Atmos. Oceanic Technol.* 22: 338 – 351, doi: 10.1175/JTECH1712.1.

Loeb, N. G., Sun, W., Miller, W. F., Loukachine, K., and Davies, R. (2006), Fusion of CERES, MISR, and MODIS measurements for top-of-atmosphere radiative flux validation, *J. Geophys. Res.*, 111, D18209, doi:10.1029/2006JD007146.

Loeb N. G., Kato S, Loukachine K, Manalo-Smith N. (2007). Angular distribution models for top-of-atmosphere radiative flux estimation from the Clouds and the Earth's Radiant Energy

System instrument on the Terra satellite. Part II: Validation. *J. Atmos. Oceanic Technol.* 24: 564 – 584, doi: 10.1175/JTECH1983.1.

Loeb, N. G., Wielicki, B. A., Doelling, D. R., Smith, G. L., Keyes, D. F., Kato, S., Manalo-Smith, N., & Wong, T. (2009). Toward Optimal Closure of the Earth's Top-of-Atmosphere Radiation Budget, *J. of Climate*, 22(3), 748-766. https://journals.ametsoc.org/view/journals/clim/22/3/2008jcli2637.1.xml

Loeb, N. G. and B.A. Wielicki (2015),SATELLITES AND SATELLITE REMOTE SENSING | Earth's Radiation Budget,Encyclopedia of Atmospheric Sciences (Second Edition), Academic Press, 2015, 67-76, https://doi.org/10.1016/B978-0-12-382225-3.00349-2.

Loeb, N. G., Doelling, D. R., Wang, H., Su, W., Nguyen, C., Corbett, J. G., Liang, L., Mitrescu, C., Rose, F. G., and Kato, S. (2018). Clouds and the Earth's Radiant Energy System (CERES) Energy Balanced and Filled (EBAF) Top-of-Atmosphere (TOA) Edition-4.0 Data Product. *J. of Climate* 31, 2, 895-918, https://doi.org/10.1175/JCLI-D-17-0208.1.

Meftah, M., Boutéraon, T., Dufour, C., Hauchecorne, A., Keckhut, P., Finance, A., et al. (2021). The UVSQ-SAT/INSPIRESat-5 CubeSat Mission: First In-Orbit Measurements of the Earth's Outgoing Radiation. *Remote Sens.*, *13*(8), 1449. https://doi.org/10.3390/rs13081449.

Rutan, D. A., Smith, G. L., & Wong, T. (2014). Diurnal Variations of Albedo Retrieved from Earth Radiation Budget Experiment Measurements. *J. of Appl. Met. and Clim.*, *53*(12), 2747–2760. http://www.jstor.org/stable/26176466.

Sardeshmukh, P. D, G. P. Compo and C. Penland (2015). Need for Caution in Interpreting Extreme Weather Statistics. *J. of climate*, *28* (23), 9166-9187. doi:10.1175/JCLI-D-15-0020.1.

Singer, C. E., Lopez-Gomez, I., Zhang, X., & Schneider, T. (2021). Top-of-Atmosphere Albedo Bias from Neglecting Three-Dimensional Cloud Radiative Effects, *J. of the Atmos. Sciences*, *78*(12), 4053-4069. https://journals.ametsoc.org/view/journals/atsc/78/12/JAS-D-21-0032.1.xml

Song, Z.; Liang, S.; Wang, D.; Zhou, Y.; Jia, A. (2018). Long-term record of top-of-atmosphere albedo over land generated from AVHRR data, *Remote Sens. Environ,* 211, 71–88.

Stephens, G., Li, J., Wild, M. *et al.* An update on Earth's energy balance in light of the latest global observations. *Nature Geosci.* **5,** 691–696 (2012). https://doi.org/10.1038/ngeo1580.

Stephens, G. L., O'Brien, D., Webster, P. J., Pilewski, P., Kato, S., and Li, J. (2015), The albedo of Earth. *Rev. Geophys.*, 53, 141– 163. doi: 10.1002/2014RG000449.

Stephens, G. L., Hakuba, M. Z., Hawcroft, M., Haywood, J. M., Behrangi, A., Kay, J. E., & Webster, P. J. (2016), The curious nature of the hemispheric symmetry of the Earth's water and energy balances. *Current Climate Change Reports*, 2(4), 135– 147. https://doi.org/10.1007/s40641-016-0043-9.

Swartz, W., Lorentz, S., Papadakis, S., Huang, P., Smith, A., Deglau, D., et al. (2019). RAVAN: CubeSat Demonstration for Multi-Point Earth Radiation Budget Measurements. *Remote Sens.*, *11*(7), 796. https://doi.org/10.3390/rs11070796.

Su, W., J. Corbett, Z. Eitzen, and L. Liang (2015a), Next-generation angular distribution models for top-of-atmosphere radiative flux calculation from CERES instruments: Methodology. *Atmos. Meas. Tech.*, 8, 611–632, doi:10.5194/amt-8-611-2015.

Su, W., Corbett, J., Eitzen, Z., and Liang, L. (2015b), Next-generation angular distribution models for top-of-atmosphere radiative flux calculation from CERES instruments: validation, *Atmos. Meas. Tech*., 8, 3297–3313, https://doi.org/10.5194/amt-8-3297-2015.

Sun, W., N. G. Loeb,R. Davies, K. Loukachine, and W. F. Miller (2006), Comparison of MISR and CERES top-of-atmosphere albedo, *Geophys. Res. Lett.*,33, L23810, doi:10.1029/2006GL027958.

Wild, M., Folini, D., Hakuba, M.Z. *et al.* (2015). The energy balance over land and oceans: an assessment based on direct observations and CMIP5 climate models. *Clim. Dyn.* **44,** 3393–3429. https://doi.org/10.1007/s00382-014-2430-z.

Zhan, C. and S. Liang (2022), Improved estimation of the global top-of-atmosphere albedo from AVHRR data, *Remote Senss. Environ.*, 269, 112836, ISSN 0034-4257, https://doi.org/10.1016/j.rse.2021.112836.

Zhan, Y.; Di Girolamo, L.; Davies, R.; Moroney, C. Instantaneous Top-of-Atmosphere Albedo Comparison between CERES and MISR over the Arctic (2018), *Remote Sens.,10*, 1882. https://doi.org/10.3390/rs10121882.

Figure captions

Figure 1. (a) PDFs of the monthly mean near-global (80S-80N) distribution of all-sky broadband TOA SW Flux (W/m^2) measured from MISR and CERES. We analyze 240 monthly samples at each grid points for 2001-2020. MISR broadband (BB) TOA SW flux (W/m^2) is converted from four narrow band albedos. The bin size is 1 W/m^2, and the total integration of the area under each PDF is normalized to be one. (b) Four narrow bands, Channel 1 - Channel 4 (C1 - C4) MISR TOA SW flux (W/m^2) centered at blue, green, red, and near-infrared. MISR broadband flux is overlaid with a black curve.

Figure 2. Deviation of PDF of MISR TOA SW flux (W/m^2) from normal distribution. The PDF is for MISR TOA SW Flux, as described in Figure 1(a). The blue curve is a best-fit lognormal distribution of the TOA SW flux values. The red curve is a best-fit normal distribution using the mean and the standard deviation of the TOA SW flux. The yellow curve is a hypothetical normal distribution with a mean at the mode of the flux distribution. The black and blue dotted line represents the mean and median value of the SW flux, respectively.

Figure 3. Difference of median and mean climatology of TOA SW flux (W/m^2) ((a)-(b)) and spatial distribution of temporal skewness ((c)-(d)) and kurtosis ((e)-(f)) of TOA SW flux from MISR and CERES.

Figure 4. PDFs of the SW flux over the (a) Deccan Peninsula and (b) central Southern Pacific ocean.

Figure 5. Scatter plot of skewness of the TOA SW flux with respect to the TOA SW flux values over the high skewness area in the central Southern Pacific ocean.

Figure 6. Annual cycles of the mean and median climatology of the SW flux (W/m^2) from MISR and CERES for near-global (left), NH (center), and SH (right). The second and third rows are NH and SH land and ocean, respectively. The filled marks represent median values of the fluxes and unfilled marks represent mean of the fluxes.

Figure 7. Differences of median climatology (2001-2020) of TOA SW flux (W/m^2) between MISR and CERES from the Terra satellite. Black and red contour lines indicate high elevation area (z>2km) and high cloud regions (cloud height> 9km), respectively.

Figure 8. PDFs of MISR and CERES SW flux (W/m^2) over the ocean for different cloud heights from 1 to 12 km.

Figure 9. The difference between two median values (CERES - MISR)/CERES in % and skewness of the TOA SW distribution over the ocean, as a function of cloud height.

Figure 10. Time series of annual mean NH and SH TOA SW fluxes from CERES EBAF, CERES-Terra, CERES-Aqua, and MISR-Terra (upper) and CERES EBAF TOA SW flux differences with various missing latitudes (lower). The poleward missing latitudes are indicated by the plot legend.

Figure 11. Local time coverage from Terra (red) and Aqua (blue) CERES. Jan 1, 2008 is used to illustrate the differences between the NH and SH sampling in local time.

Table Caption

Table 1. Annual mean TOA reflected SW flux (W/m^2) from 2001-2020 for different regions from MISR, CERES SSF, and CERES EBAF products. Numbers in parenthesis are calculated with zonal median, instead of zonal mean.

Figure 1.

PDFs of GLOBAL ALL-SKY TOA SW FLUX

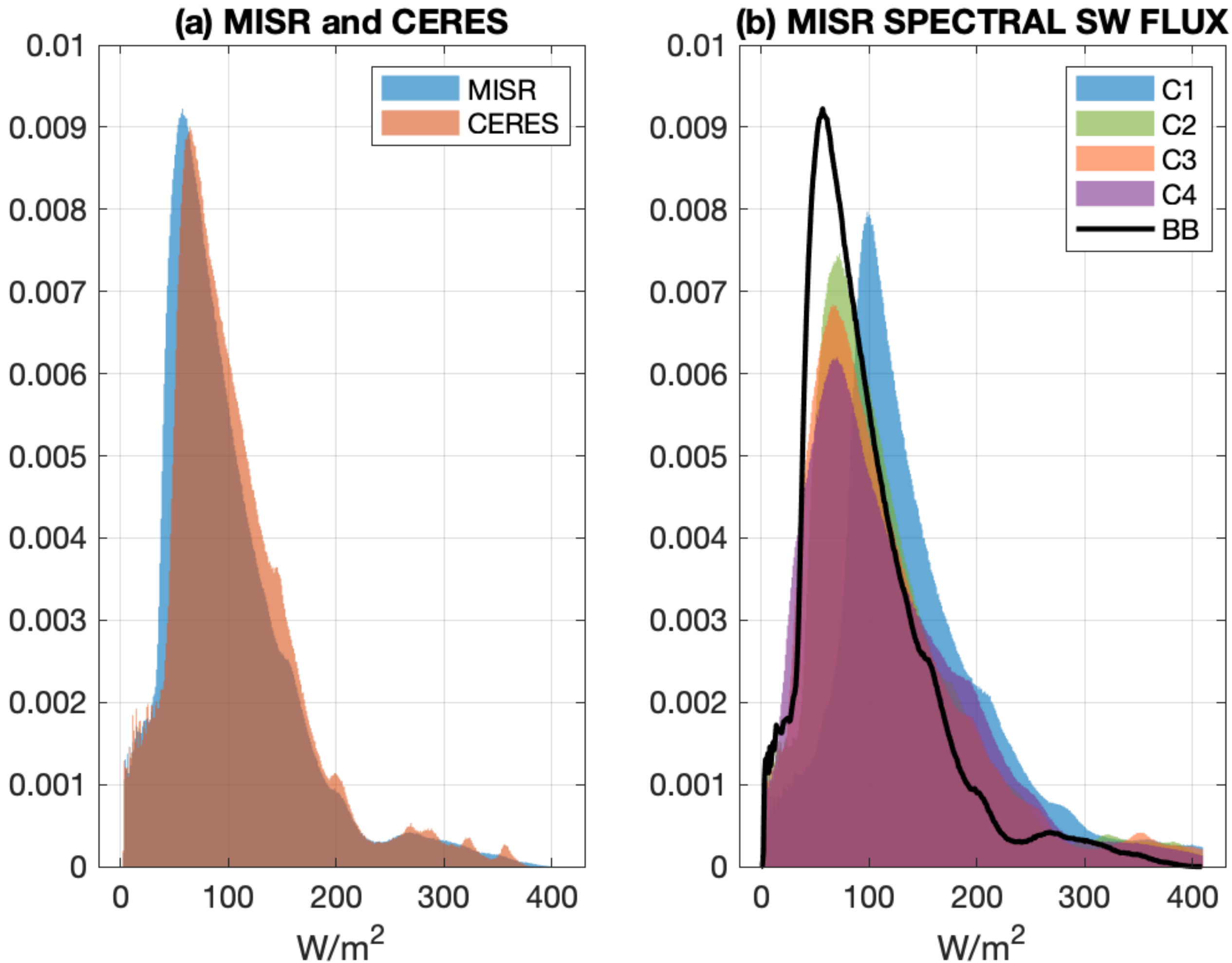

Figure 2.

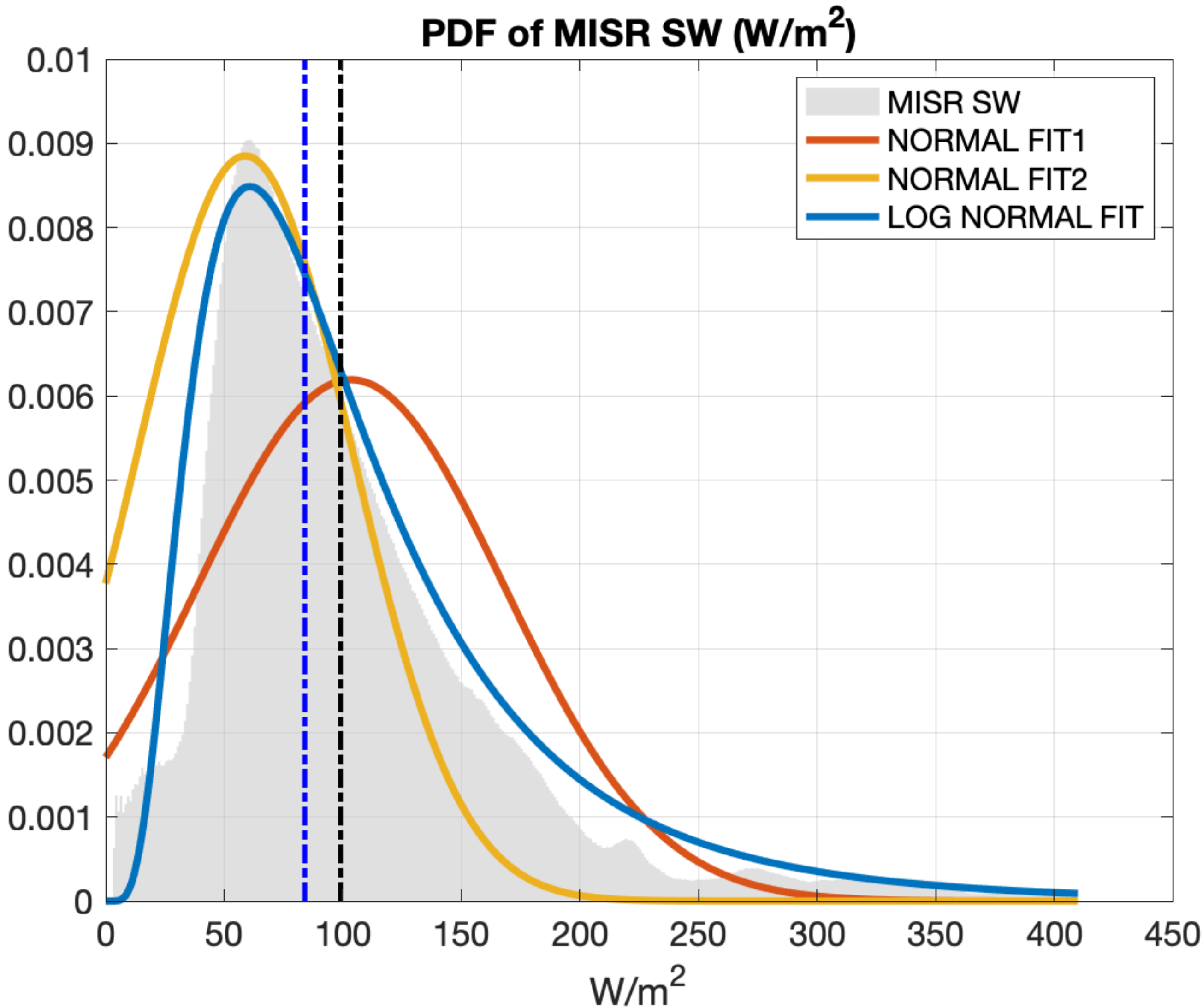
PDF of MISR SW (W/m²)
MISR SW
NORMAL FIT1
NORMAL FIT2
LOG NORMAL FIT
0.01
0.009
0.008
0.007
0.006
0.005
0.004
0.003
0.002
0.001
0
0
50
100
150
200
250
300
350
400
450
W/m²

Figure 3.

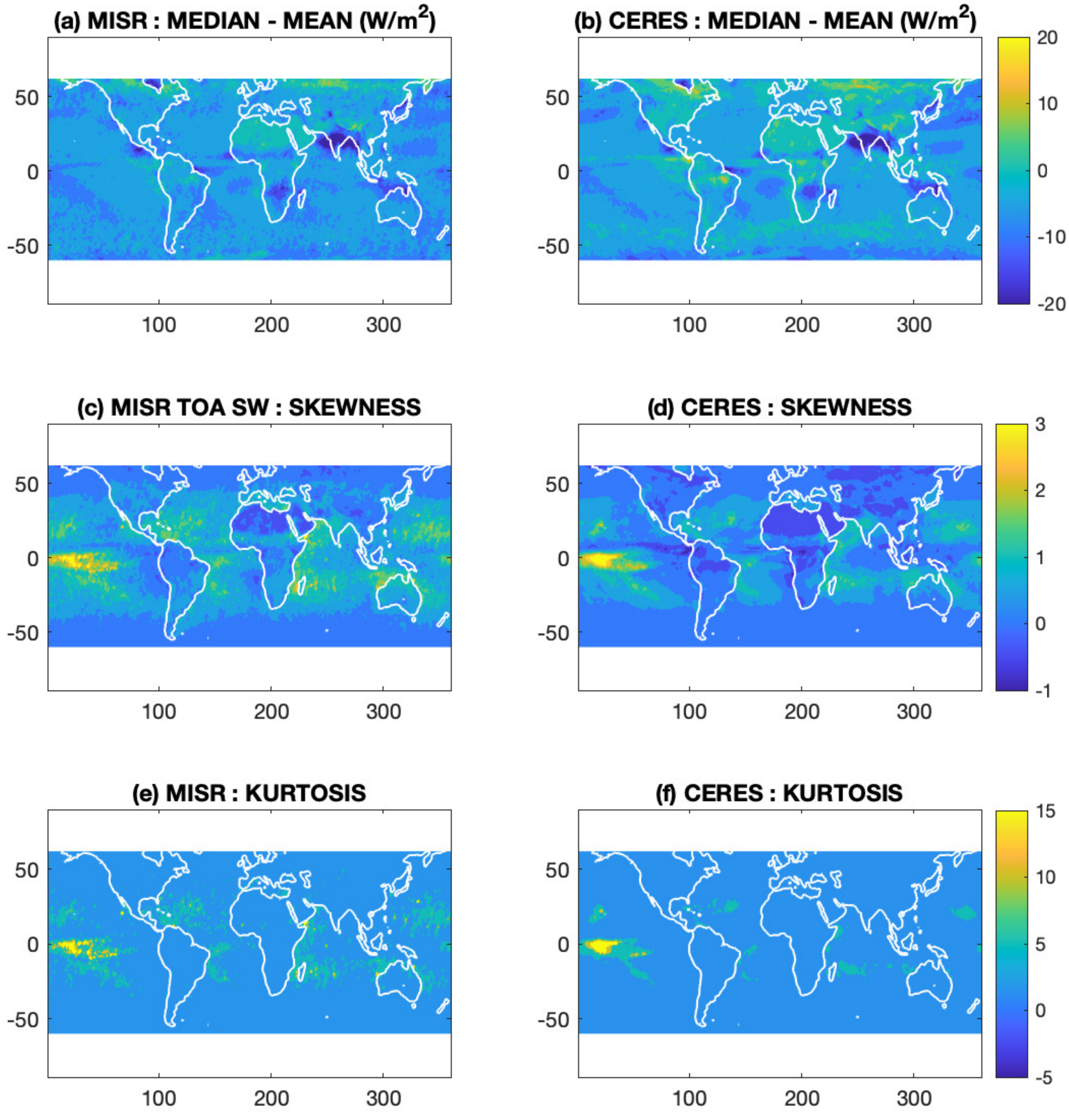

(a) MISR : MEDIAN - MEAN (W/m2)
(b) CERES : MEDIAN - MEAN (W/m2)
(c) MISR TOA SW : SKEWNESS
(d) CERES : SKEWNESS
(e) MISR : KURTOSIS
(f) CERES : KURTOSIS
50
0
-50
100
200
300
20
10
0
-10
-20
3
2
1
0
-1
15
10
5
0
-5

Figure 4.

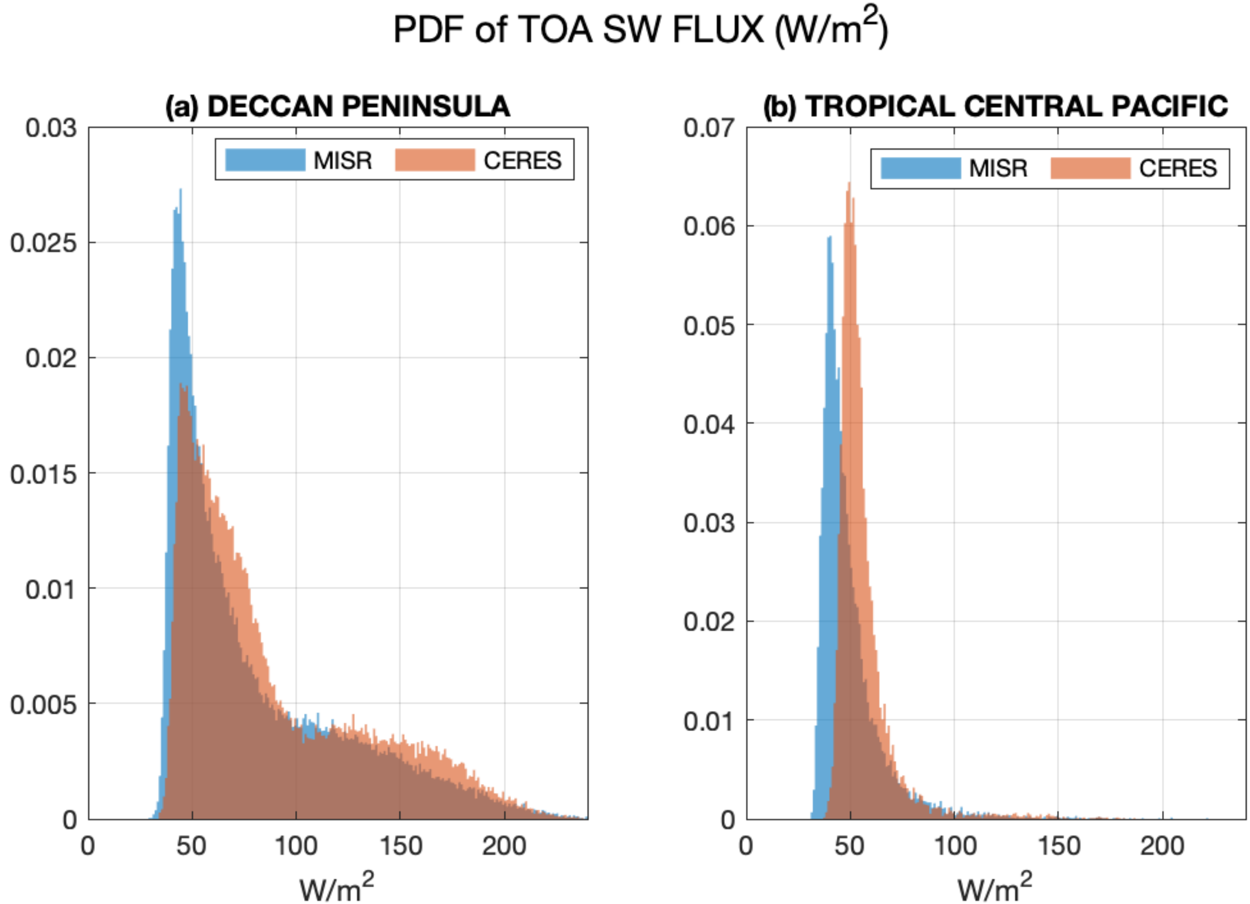
PDF of TOA SW FLUX (W/m^2)
(a) DECCAN PENINSULA
MISR
CERES
0.03
0.025
0.02
0.015
0.01
0.005
0
0
50
100
150
200
W/m^2
(b) TROPICAL CENTRAL PACIFIC
MISR
CERES
0.07
0.06
0.05
0.04
0.03
0.02
0.01
0
0
50
100
150
200
W/m^2

Figure 5.

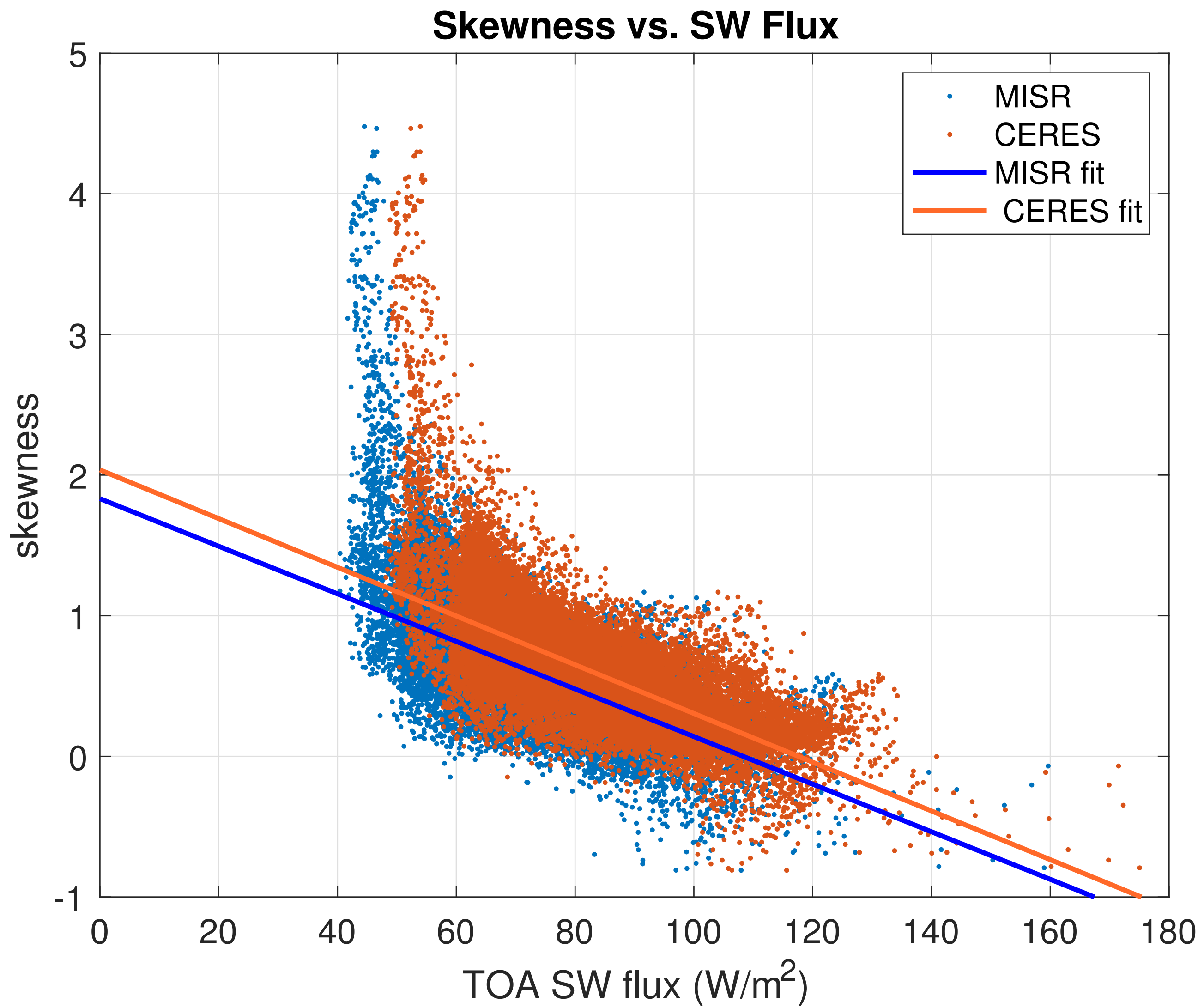

Skewness vs. SW Flux
MISR
CERES
MISR fit
CERES fit
skewness
TOA SW flux (W/m^2)
5
4
3
2
1
0
-1
0
20
40
60
80
100
120
140
160
180

Figure 6.

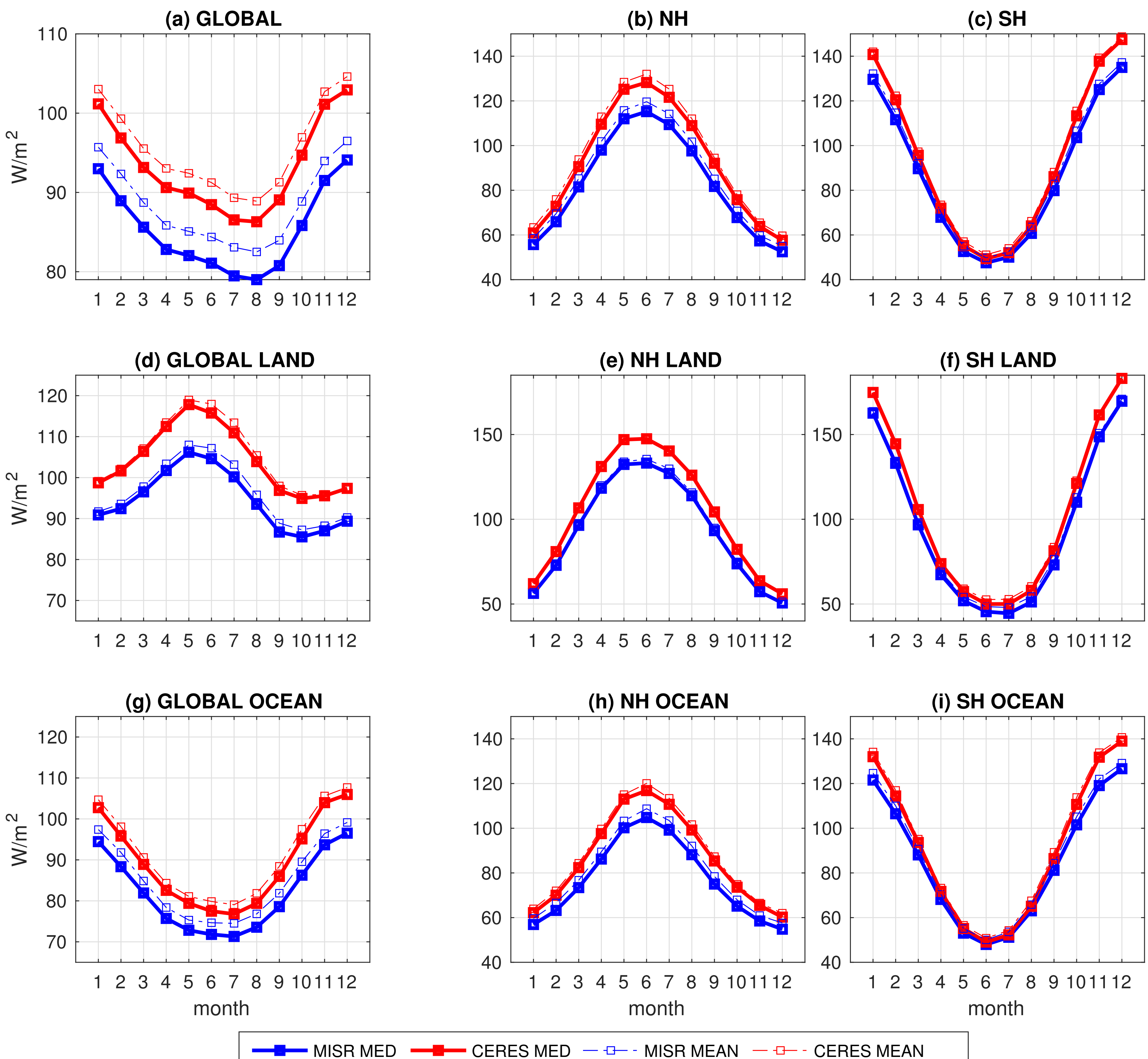
(a) GLOBAL
(b) NH
(c) SH
(d) GLOBAL LAND
(e) NH LAND
(f) SH LAND
(g) GLOBAL OCEAN
(h) NH OCEAN
(i) SH OCEAN
W/m2
month
MISR MED
CERES MED
MISR MEAN
CERES MEAN

Figure 7.

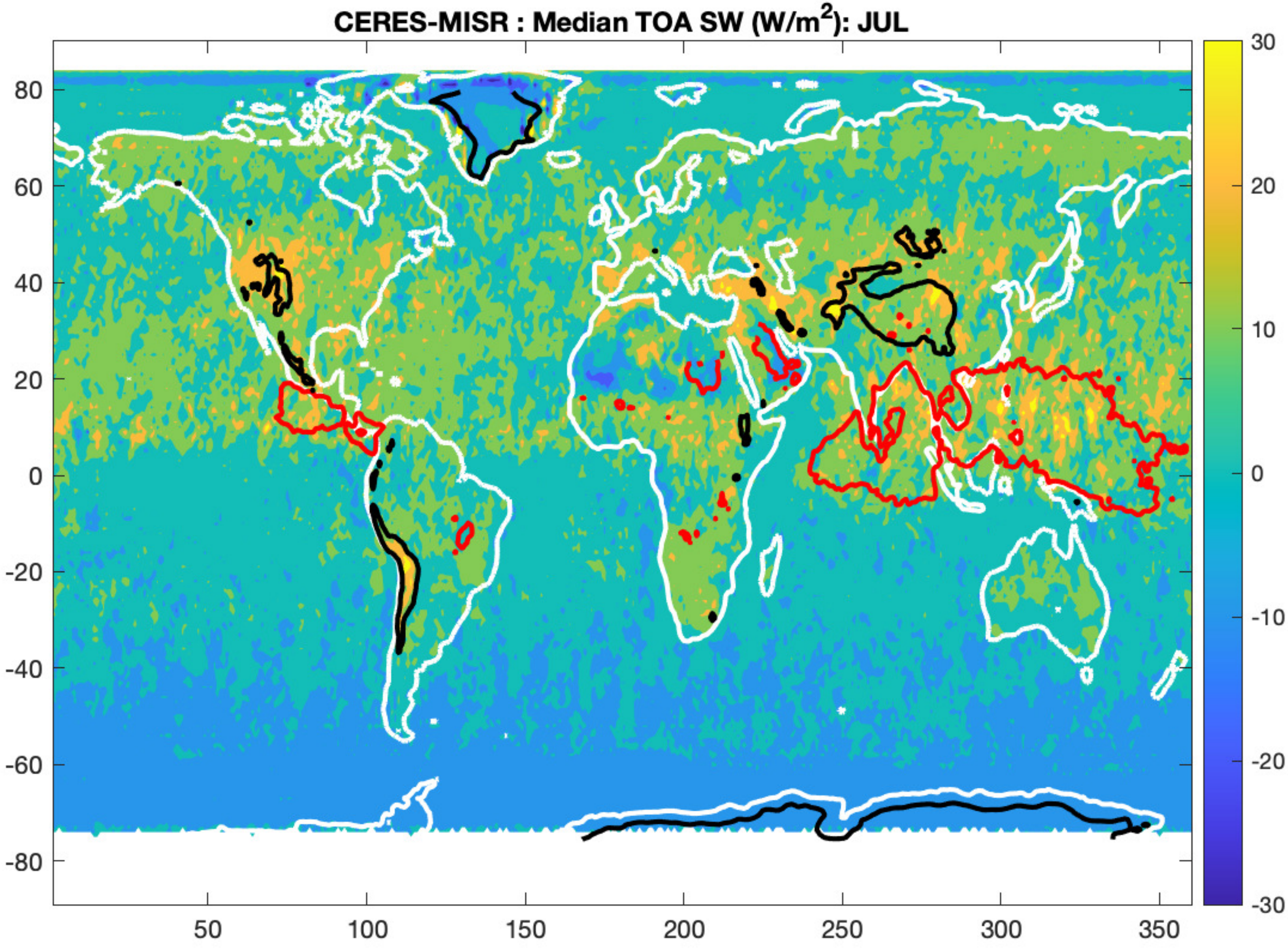

CERES-MISR : Median TOA SW (W/m2): JUL
80
60
40
20
0
-20
-40
-60
-80
50
100
150
200
250
300
350
30
20
10
0
-10
-20
-30

Figure 8.

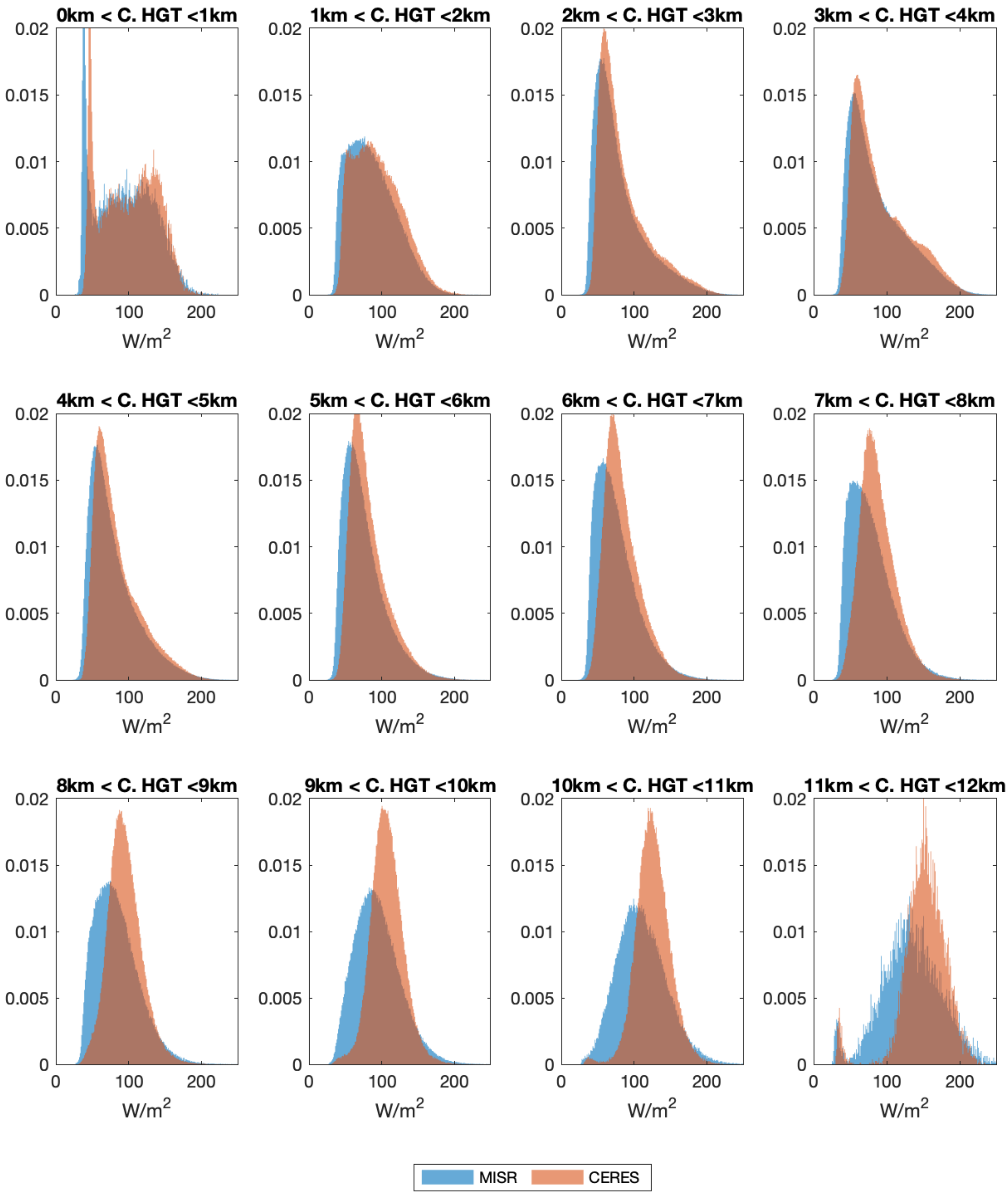
0km < C. HGT <1km
1km < C. HGT <2km
2km < C. HGT <3km
3km < C. HGT <4km
4km < C. HGT <5km
5km < C. HGT <6km
6km < C. HGT <7km
7km < C. HGT <8km
8km < C. HGT <9km
9km < C. HGT <10km
10km < C. HGT <11km
11km < C. HGT <12km
0.02
0.015
0.01
0.005
0
0
100
200
W/m2
MISR
CERES

Figure 9.

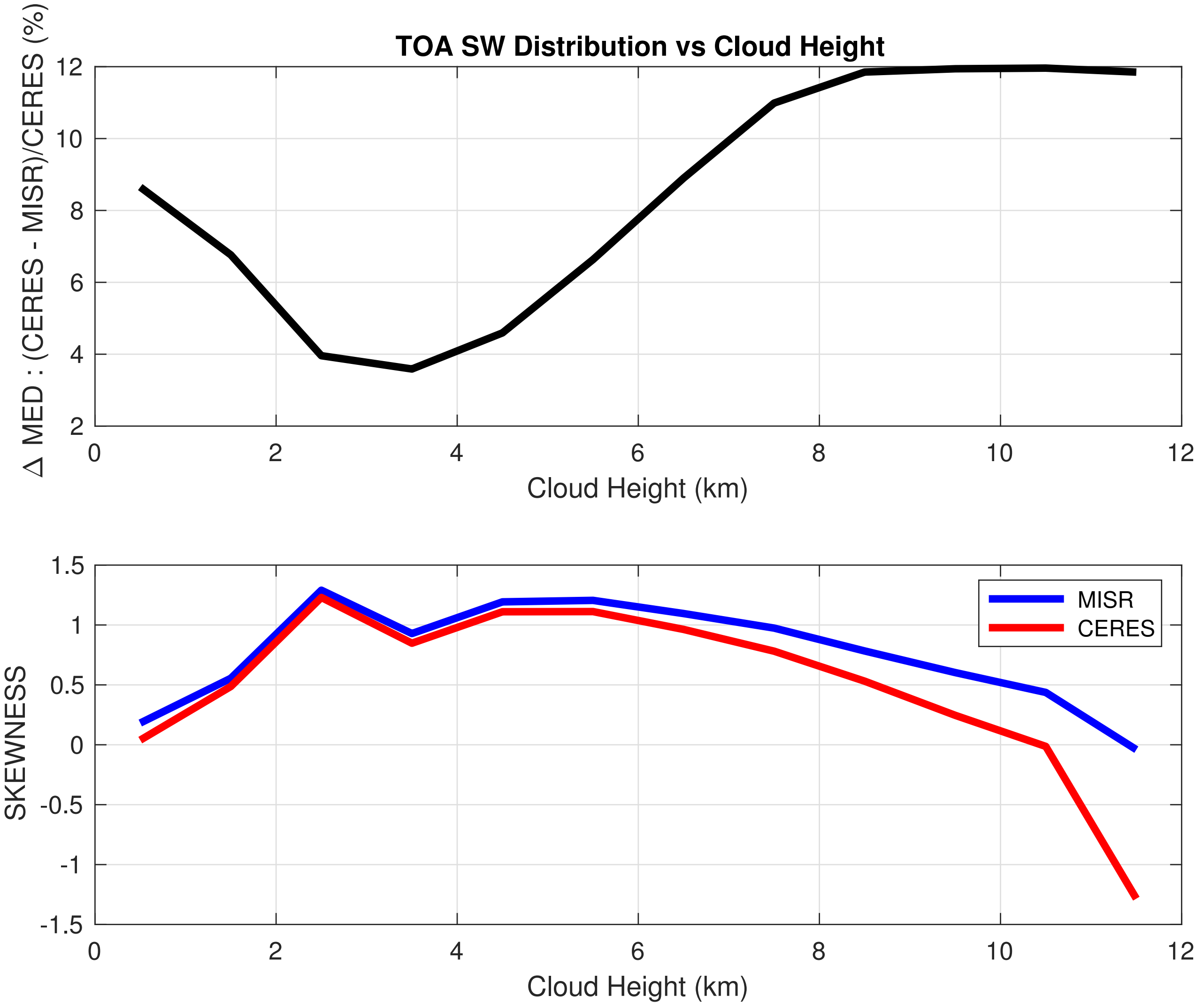
TOA SW Distribution vs Cloud Height
Δ MED : (CERES - MISR)/CERES (%)
2
4
6
8
10
12
0
2
4
6
8
10
12
Cloud Height (km)
SKEWNESS
1.5
1
0.5
0
-0.5
-1
-1.5
MISR
CERES
0
2
4
6
8
10
12
Cloud Height (km)

Figure 10.

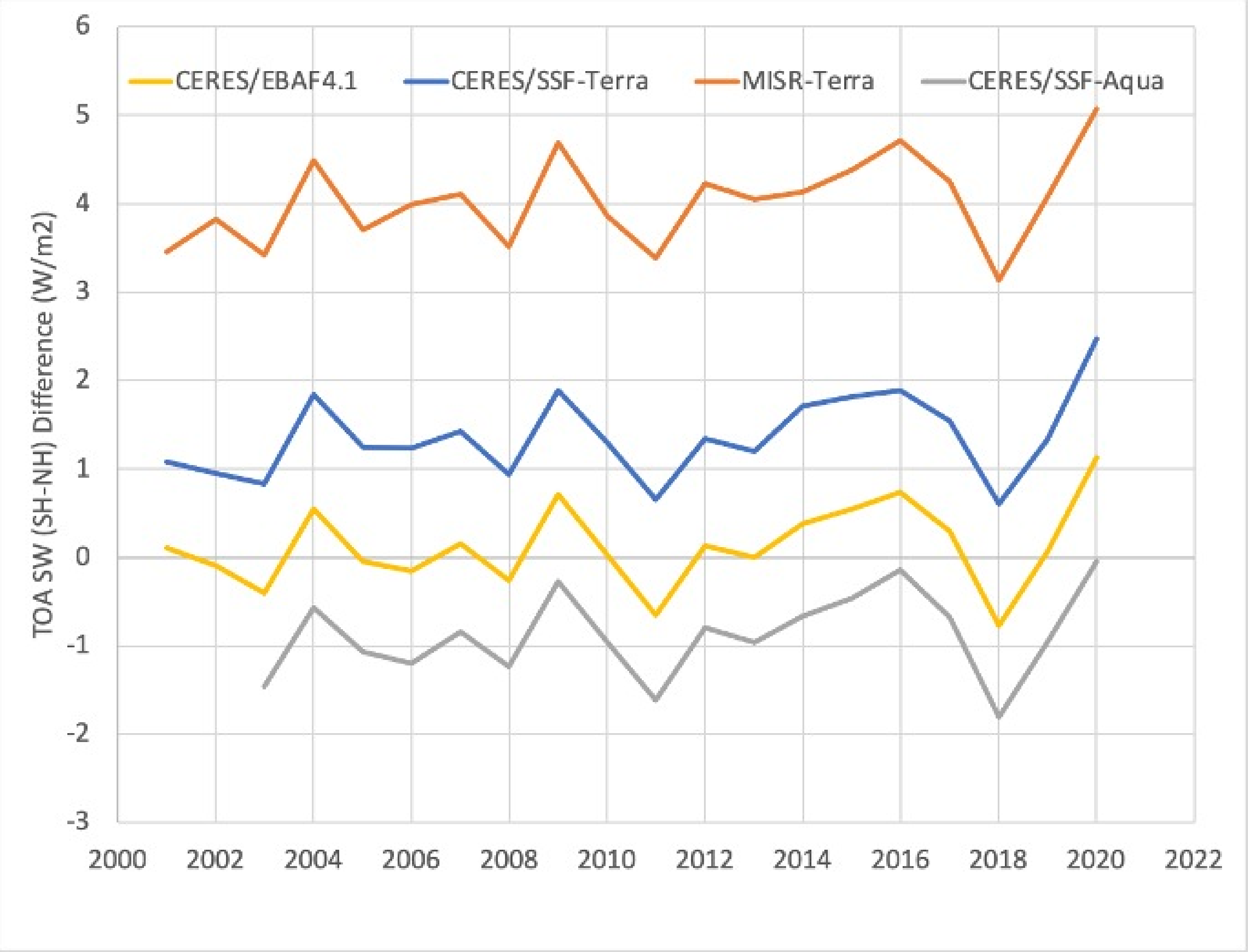
CERES/EBAF4.1
CERES/SSF-Terra
MISR-Terra
CERES/SSF-Aqua
TOA SW (SH-NH) Difference (W/m2)
6
5
4
3
2
1
0
-1
-2
-3
2000
2002
2004
2006
2008
2010
2012
2014
2016
2018
2020
2022

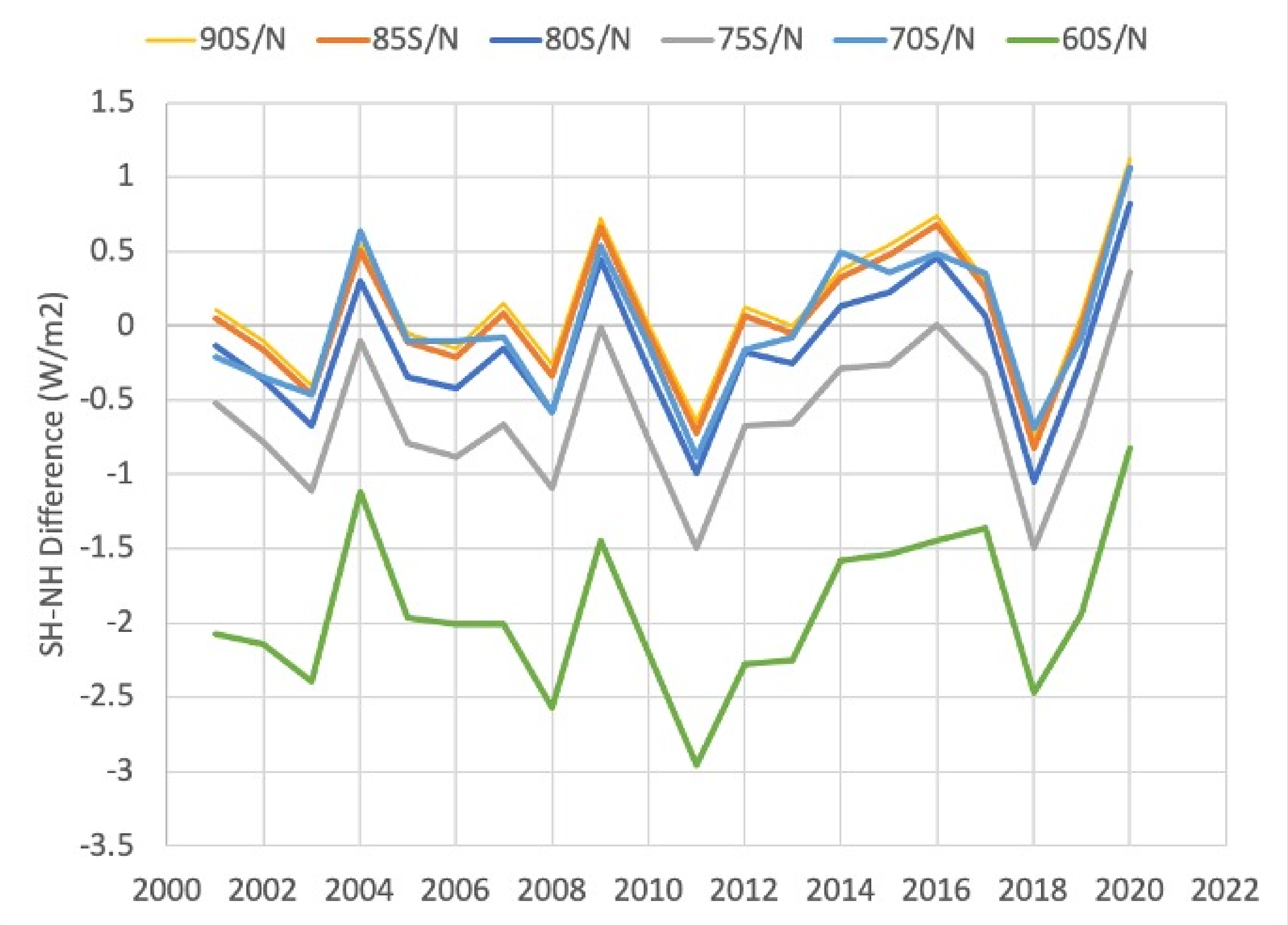
90S/N
85S/N
80S/N
75S/N
70S/N
60S/N
SH-NH Difference (W/m2)
1.5
1
0.5
0
-0.5
-1
-1.5
-2
-2.5
-3
-3.5
2000
2002
2004
2006
2008
2010
2012
2014
2016
2018
2020
2022

Figure 11.

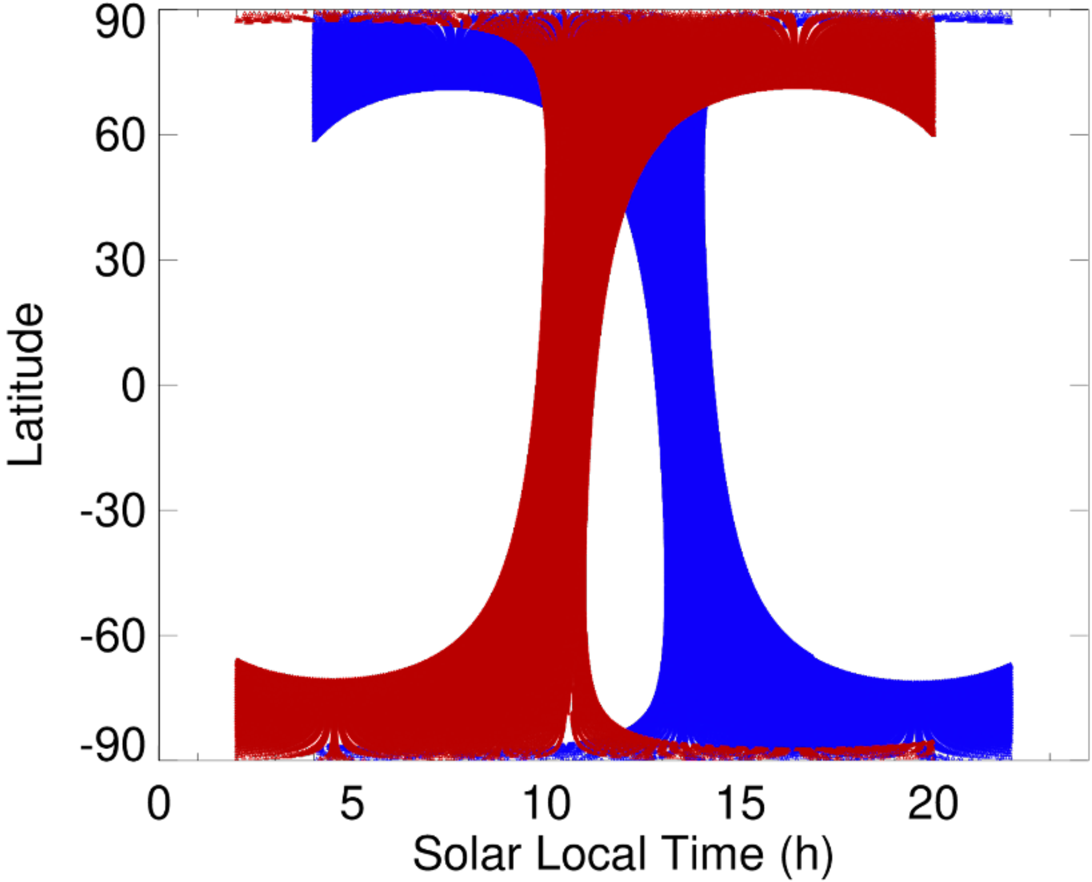
Latitude
90
60
30
0
-30
-60
-90
0
5
10
15
20
Solar Local Time (h)

Table 1

	MISR (W/m^2) (80S-80N)	CERES SSF(W/m^2) (80S-80N)	CERES SSF (W/m^2) (90S-90N)	CERES EBAF (W/m^2) (90S-90N)
Global	88.41 (85.34)	95.68 (93.40)	96.26 (93.98)	99.04 (96.92))
NH	86.43 (82.88)	95.11 (92.26)	95.53 (92.67)	98.94 (96.29)
SH	90.35 (87.76)	96.26 (94.52)	96.99 (95.27)	99.14 (97.54)
SH - NH	3.92 (4.89)	1.15 (2.26)	1.47 (2.60)	0.20 (1.60)
LAND	96.26 (94.55)	105.37 (104.35)	105.38 (104.37)	110.36 (109.52)
OCEAN	85.05 (82.08)	91.56 (89.51)	91.59 (89.53)	94.21 (92.18)
NH LAND	95.21 (93.76)	104.89 (103.98)	104.90 (103.99)	108.18 (107.31)
SH LAND	98.45 (96.19)	106.36 (105.16)	105.14 (104.90)	114.87 (114.10)
NH OCEAN	80.40 (77.12)	88.39 (86.38)	88.44 (86.44)	92.59 (90.62)
SH OCEAN	88.42 (85.66)	93.84 (91.76)	93.86 (91.77)	95.38 (93.31)